Distinct regions of *H. pylori's* bactofilin regulate protein interactions to control cell shape

Sophie R Sichel[1, 2], Benjamin P Bratton[3, 4], and Nina R Salama[2 *]

1. Molecular Medicine and Mechanisms of Disease Graduate Program, University of Washington, Seattle, WA, 98195, United States
2. Division of Human Biology, Fred Hutchinson Cancer Center, Seattle, WA, 98109, United States
3. Department of Pathology, Microbiology and Immunology, Vanderbilt University Medical Center, Nashville, TN 37232, United States
4. Vanderbilt Institute for Infection, Immunology and Inflammation, Nashville, TN 37232, United States

Corresponding author *

Key words: Bactofilin / cell shape / cytoskeleton / *H. pylori* / peptidoglycan

Character count: 51,570

Abstract

Chronic infection of the stomach with the bacterium *Helicobacter pylori* can cause gastric cancers and ulcers, and the helical shape of *H. pylori* cells promotes stomach colonization. A helical shape promoting protein complex includes peptidoglycan-hydrolases, a peptidoglycan precursor synthesis enzyme, non-enzymatic transmembrane proteins, and the cytoplasmic bactofilin CcmA. Bactofilins are highly conserved spontaneously polymerizing cytoskeletal proteins in bacteria. Using a combination of CcmA deletion analysis, *in vitro* polymerization, and *in vivo* co-immunoprecipitation experiments we show that the bactofilin domain and N-terminal region of CcmA are required for helical cell shape and the bactofilin domain is sufficient for polymerization and interactions with transmembrane proteins Csd5 and Csd7. The CcmA N-terminal region inhibits interaction with Csd7. Deletion of the N-terminal region of CcmA increases CcmA-Csd7 interactions and destabilizes the peptidoglycan-hydrolase Csd1. Using super-resolution microscopy, we found that Csd5 recruits CcmA to the cell envelope and promotes CcmA enrichment at the major helical axis. Thus, a combination of CcmA protein-protein and interpolymer interactions regulate CcmA localization and peptidoglycan-hydrolase stability to generate the helical shape of *H. pylori* cells.

Introduction

Helicobacter pylori is a helical-shaped, Gram-negative bacteria that infects more than half of the world's population (Hooi *et al*, 2017). Chronic infection with *H. pylori* can cause

gastric ulcers and cancers; approximately 80% of gastric cancer cases are attributed to *H. pylori* infection (de Martel *et al*, 2020). The helical shape of *H. pylori* cells helps establish colonization of the stomach and promotes immunopathology during infection (Martinez *et al*, 2018; Montecucco & Rappuoli, 2001; Sycuro *et al*, 2010; Sycuro *et al*, 2012; Yang *et al*, 2019). Multiple proteins have been identified that are essential for the helical shape of *H. pylori* cells, all of which influence the shape and composition of the peptidoglycan (PG) sacculus directly or indirectly (Sycuro *et al.*, 2010; Sycuro *et al*, 2013; Sycuro *et al.*, 2012; Yang *et al.*, 2019).

Several cell-shape-determining (Csd) proteins form a membrane-spanning protein complex. CcmA is proposed to interact with the integral membrane protein Csd7, which stabilizes the PG-hydrolase Csd1 and Csd2, a catalytically inactive homologue of Csd1 (Yang *et al.*, 2019). CcmA also interacts with the transmembrane protein Csd5, which has an SH3 domain that binds to PG. Csd5 also interacts with ATP synthase and MurF, an essential PG precursor enzyme that catalyzes the final cytoplasmic PG biosynthesis step independent of interactions with CcmA (Blair *et al*, 2018; Hrast *et al*, 2013). CcmA and probes that report on PG synthesis localize to the major helical axis of *H. pylori* cells (regions with a Gaussian curvature value of 5 ±1 μm^{-2} on a helical cell) indicating that CcmA is in the same region of the cell where PG synthesis occurs (Taylor *et al*, 2020).

CcmA is the only bactofilin encoded in the *H. pylori* genome, a class of highly conserved, spontaneously-polymerizing, cytoskeletal proteins in bacteria. Bactofilins perform a variety of functions (Bulyha *et al*, 2013; El Andari *et al*, 2015; Lin *et al*, 2017; Osorio-Valeriano *et al*, 2019) including modulating cell shape (Brockett *et al*, 2021; Hay *et al*, 1999; Jackson *et al*, 2018; Koch *et al*, 2011; Sycuro *et al.*, 2010) and morphogenesis

of cell appendages (Billini *et al*, 2019; Caccamo *et al*, 2020; Kuhn *et al*, 2010). They are identified by the presence of a bactofilin domain (DUF583) which forms a β-helix and is flanked by unstructured terminal regions. It has been proposed that the terminal regions may be involved in modulating polymerization, binding to membranes and/or interacting with other proteins (Deng *et al*, 2019; Kuhn *et al.*, 2010; Vasa *et al*, 2015).

We performed structure-function analysis to determine how the bactofilin domain and the terminal regions of CcmA contribute to generating the helical shape of *H. pylori* cells by evaluating cell morphology, CcmA polymerization and filament bundling, and interaction with known Csd protein interaction partners. Additionally, we identified how protein binding partners impact CcmA localization. We found that polymer bundling and interactions between CcmA and other Csd proteins are responsible for CcmA's ability to pattern the helical shape of *H. pylori* cells via protein localization and modulation of the PG-hydrolase Csd1 protein stability.

Results

CcmA is composed of a bactofilin domain and two short terminal regions

We identified the functional regions of CcmA by aligning the amino acid sequence of CcmA with BacA, a well-studied bactofilin from *C. crescentus* involved in stalk morphogenesis, using Swiss-Model (Waterhouse *et al*, 2018) and found that CcmA is composed of a bactofilin domain (DUF 583) surrounded by two short terminal regions (Figure 1A). The N-terminal region is composed of amino acids 1-17, the bactofilin domain is composed of amino acids 18-118, and the C-terminal region is composed of amino

acids 119-136. Deng and colleagues proposed that bactofilins may contain a short membrane binding motif within their N-terminal regions and in CcmA that motif spans amino acids 3-12 (Deng *et al.*, 2019). After identifying the boundaries between the bactofilin domain and the terminal regions of CcmA we used RoseTTAFold (Baek *et al*, 2021), a protein structure prediction service that uses deep learning-based modeling methods, to predict the structure of CcmA. RoseTTAFold generated five models of CcmA. In all five, the bactofilin domain forms a three-sided, right-handed β-helix with a left-handed twist (Figure 1B), the N-terminal region is unstructured, and part of the C-terminal region forms a short α-helix and caps the end of the bactofilin domain (Figure 1C). In four of the five models, the first several amino acids of the N-terminal region interact with the bactofilin domain suggesting that the N-terminal region could potentially block a surface of the bactofilin domain.

The N-terminal region and bactofilin domain are together necessary and sufficient to pattern the helical shape of *H. pylori* cells

To identify the role of each domain/region of CcmA we generated *H. pylori* strains that have truncated versions of *ccmA* at the native c*cmA* locus. We generated five strains, one strain missing the N-terminal region (Δ*NT*, missing amino acids 2-17), another strain missing the proposed membrane binding motif within the N-terminus (Δ*MM*, missing amino acids 3-12), a third strain lacking the five amino acids at the end of the N-terminus (Δ*13-17*, lacking amino acids 13-17), a fourth strain missing the C-terminal region (Δ*CT*, missing amino acids 119-136), and lastly, a strain expressing only the bactofilin domain lacking both the N-terminal region and C-terminal region (BD, expressing amino acids 18-

118) (Figure 2A). The open reading frames (ORF) of the end of *csd1* and the beginning of *ccmA* overlap by 82 nucleotides (Sycuro *et al.*, 2010), thus to avoid impacting the function Csd1 by removing several amino acids from the C-terminus of Csd1 while truncating the N-terminus of CcmA, we expressed a second copy of *csd1* at *rd*xA, a locus commonly used for complementation (Smeets *et al*, 2000). In previous work, we confirmed that both CcmA and Csd1 can be individually deleted and complemented back without impacting the expression of the other (Sycuro *et al.*, 2010; Yang *et al.*, 2019).

All strains expressed the truncated versions of CcmA measured by western blotting with an α-CcmA polyclonal antibody, however, in strains lacking the C-terminus (Δ*CT* and BD) we saw much lower signal on the blot (Figure 2B). In follow-up experiments to determine whether the α-CcmA polyclonal antibody fails to recognize versions of CcmA lacking the C-terminus, (Expanded view Figure 1) we ran a western blot probed with our polyclonal α-CcmA antibody on purified 6-his WT CcmA and CcmA truncation mutants (Expanded View Figure 2). Although equal concentrations of each purified protein were loaded, the polyclonal α-CcmA antibody poorly recognized versions of CcmA lacking the C-terminal region (Δ*CT* and BD), suggesting that the Δ*CT* and BD proteins are likely expressed in *H. pylori* cells at similar levels to other versions of CcmA but are not robustly recognized by the α-CcmA polyclonal antibody.

Next, after confirming that all truncated versions of CcmA were expressed, we assessed the shapes of the cells and found that strains lacking the N-terminal region (Δ*NT* and BD) were indistinguishable from Δ*ccmA* cells (Figure 2 C-D), while cells lacking the C-terminal region of *ccmA* resembled WT cells. Cells that lacked either the putative membrane binding motif (Δ*MM*) or the last five amino acids of the N-terminal region (Δ*13*-

17) were helical but had slightly different side curvature values than the WT population, suggesting that the N-terminal region of CcmA may have multiple functional regions within it.

Circular dichroism spectroscopy suggests that the secondary structure of WT CcmA is primarily β-strands

Circular dichroism (CD) spectroscopy can be used to identify the secondary structure and folding of proteins. Different structural elements have characteristic CD spectra and proteins that consist of β-strands have negative peaks at 216 nm (Greenfield, 2006). We sought to identify whether CcmA is composed of β-strands and confirm that our truncated versions of CcmA were still folded correctly, especially considering that in *H. pylori* strains lacking the N-terminal region of CcmA, cells resembled Δ*ccmA* mutants. We recombinantly expressed and purified 6-his CcmA (Expanded View Figure 2) and collected circular dichroism spectra from 200-260 nm at fixed temperatures to identify the secondary structure and measure its thermal stability.

CD spectra of WT CcmA and the truncation mutants Δ*NT*, Δ*CT*, and BD at 20 ºC all look very similar; they have the characteristic negative peak at 216 nm indicating β-strand secondary structure (Figure 3A). Together, these data combined with the modeling by RoseTTAFold in Figure 1C suggest that CcmA's bactofilin domain very likely forms a β-helix. In contrast, we also ran CD scans on WT CcmA at 95 ºC and two CcmA point mutants that our group previously studied, I55A and L110S at 20 ºC (Taylor *et al.*, 2020). The CD spectra of both mutants (I55A and L110S) at 20 ºC resemble spectra of melted WT CcmA at 95 ºC (Figure 3B), suggesting that these proteins are not folded. Thus, while

CcmA Δ*NT*, BD, I55A, and L110S all have the same cell shape phenotype when expressed in *H. pylori* - loss of helical cell shape - the mechanism differs. In CcmA I55A and L110S, CcmA is not folded and nonfunctional, while in CcmA Δ*NT* and BD, the protein is folded, but loss of the N-terminus causes a loss of helical cell shape.

The bactofilin domain alone is capable of polymerization; the terminal regions of CcmA modulate lateral interactions between CcmA filaments

To identify how each domain/region of CcmA contributes to *in vitro* polymerization we expressed and purified truncated versions of 6-his CcmA and assessed polymerization by negative stain and transmission electron microscopy (TEM). As previously reported (Holtrup *et al*, 2019; Taylor *et al.*, 2020), WT CcmA polymerizes into small filaments that measure on average 3.04 nm (SD= 0.79, n=18) in width. The filaments wrap together to form bundles of approximately 21.34 nm (SD= 4.82, n=24) wide, and form lattice structures (Figure 4 A, G). Δ*NT* formed filaments and bundles which were more homogenous, straighter, and thinner than WT and appear to only contain 2-4 filaments each. Δ*NT* failed to form lattice structures (Figure 4B). Δ*MM* resembled WT CcmA, forming filaments and bundles of approximately the same width as WT and formed lattices (Figure 4C, G). Δ*13-17* resembled Δ*NT* (Figure 4D, G), suggesting that amino acids 13-17 may be responsible for filament bundling properties of Δ*NT*. Δ*CT* formed bundles that were wider than WT CcmA but failed to form lattices (Figure 4E, G). Lastly, BD formed straight bundles that were narrower than those found in WT samples, and failed to form lattices (Figure 4F, G). These data suggest that the bactofilin domain is sufficient for polymerization of CcmA while the N- and C-terminal regions of CcmA

regulate inter-polymer interactions that impact the width of bundles by modulating the number of filaments that form a bundle, and the ability of CcmA to form lattices.

CcmA's bactofilin domain mediates interactions with Csd5 and Csd7, and the N-terminal region of CcmA inhibits interactions with Csd7

CcmA was previously shown to interact with two Csd proteins, Csd5 and Csd7, by co-immunoprecipitation experiments followed by mass spectrometry (Blair *et al.*, 2018; Yang *et al.*, 2019). To probe how each region of CcmA contributes to interactions with Csd5 and Csd7, we performed co-immunoprecipitation experiments followed by western blotting. Strains were generated that expressed truncated versions of *ccmA* at the native *ccmA* locus, *csd1* at the *rdxA* locus as described earlier, and either *csd5-2X-FLAG* or *csd7-3X-FLAG* at their native loci. We immunoprecipitated either Csd5-FLAG or Csd7-FLAG with α-FLAG agarose beads, then performed western blotting and probed with the α-CcmA polyclonal antibody to identify whether the truncated versions of CcmA could still co-purify. We found that all truncated versions of CcmA could still co-purify with Csd5-FLAG (Figure 5A), suggesting that the bactofilin domain mediates interactions between CcmA and Csd5-FLAG. When we immunoprecipitated Csd7-FLAG we found that, as previously reported (Yang *et al.*, 2019), WT CcmA was not able to be detected in the IP fractions by western blotting above background levels. However, versions of CcmA lacking the N-terminal region were robustly co-purified by Csd7 (Figure 5B) suggesting that the N-terminal region inhibits WT CcmA from being co-immunoprecipitated by Csd7-FLAG. Additionally, we tagged WT CcmA, Δ*CT* and BD with a HaloTag in *H. pylori* at the native *ccmA* locus and performed a co-immunoprecipitation experiment to detect

interactions with Csd5-FLAG (Expanded View Figure 3). We found that both Δ*CT*-HaloTag and BD-HaloTag were expressed at comparable levels as CcmA-HaloTag and could be pulled down by Csd5-FLAG. Together these data suggest that the bactofilin domain of CcmA mediates interaction with Csd5 and Csd7, the N-terminal region of CcmA inhibits interaction with Csd7, and versions of CcmA lacking the C-terminal region are expressed at comparable levels to WT CcmA although they are not recognized as robustly by the α-CcmA polyclonal antibody.

Csd1 levels are depleted in strains lacking the N-terminal region of CcmA

After discovering that the N-terminal region of CcmA could inhibit interactions with Csd7 and that Δ*NT* CcmA was readily co-purified by Csd7, we reasoned that Δ*NT* CcmA could be binding to Csd7 and reducing its capacity to stabilize Csd1, causing decreased levels of Csd1 expression. This hypothesis was bolstered by the finding that Δ*csd7,* Δ*csd1*, and Δ*NT* cells all share the same curved rod shape phenotype. To test this hypothesis, we assayed Csd1 expression by western blotting and probing with an α-Csd1 polyclonal antibody in whole cell lysates of *H. pylori* strains expressing truncated versions of *ccmA*. As discussed previously, the strains express two copies of Csd1; they have an extra copy of *csd1* at *rdxA* which was added to account for potentially impacting Csd1's function when truncating *ccmA* (the ORF of the end of *csd1* and the beginning of *ccmA* overlap by 82 nucleotides). Strikingly, we found that in strains lacking the N-terminal region (Δ*NT* and BD) Csd1 levels are lower than WT. In Δ*NT* and BD strains, Csd1 levels are lower overall and multiple smaller bands are detected by the α-Csd1 polyclonal antibody than would be predicted based on the molecular weight of Csd1 after deleting several amino

acids from the C-terminal end of Csd1 in the *ccmA* truncation mutants (the predicted shift in molecular weight of Csd1 after truncating the NT region of CcmA is 1.91 kDa) (Figure 6). Based on these results it is likely that in strains lacking the N-terminal region of CcmA the bactofilin domain of CcmA binds to Csd7 and prevents Csd7 from stabilizing Csd1, resulting in lower levels of Csd1. Our data suggest that Csd1 stability is indirectly regulated by CcmA via Csd7 through an unknown mechanism.

CcmA requires binding partners for proper localization to the major helical axis

It has been hypothesized that bactofilins are able to interact with the cell envelope directly and sense specific curvature values. To address whether binding partners are required to direct CcmA to the cell envelope, we first engineered an *H. pylori* strain we could use to visualize CcmA. We engineered a strain with *ccmA-HaloTag* at the native *ccmA* locus and a second copy of WT *ccmA* at *rdxA*, because we found that cells with a second copy of *ccmA* at *rdxA* more closely resembled the shape of WT cells than when *ccmA-HaloTag* was the only copy of *ccmA* expressed (Expanded View Figure 4). To identify whether CcmA is capable of localizing to the cell envelope at its preferred curvature alone or whether localization is mediated by a binding partner, we deleted *csd5* and *csd7* individually and together in our *ccmA-HaloTag* strain. As an additional control we deleted *csd6* in the *ccmA-HaloTag* strain. Csd6 is a peptidoglycan carboxypeptidase that does not appear to interact with CcmA, Csd5, or Csd7 (Blair *et al.*, 2018; Sycuro *et al.*, 2013; Yang *et al.*, 2019). Similar to Δ*csd5* mutants, Δ*csd6* mutants show a straight rod shape phenotype. We fixed and permeabilized cells, then labeled CcmA-HaloTag with a fluorescent ligand (JF-549) that binds to HaloTag and counterstained with

fluorescent wheat germ agglutinin (WGA) to label the cell envelope. We collected images of hundreds of cells from each population using 3D structured illumination microscopy (SIM) and used software previously described to generate 3D reconstructions of individual cells from the WGA channel and calculate the Gaussian curvature at each point on the cell surface. Then we performed analysis to identify how much CcmA-HaloTag signal was at the cell envelope versus in the center of cells, and curvature enrichment analysis to investigate whether CcmA-HaloTag is enriched or depleted at specific Gaussian curvature values (Bratton *et al*, 2019; Taylor *et al.*, 2020).

In WT cells, we found that CcmA-HaloTag signal is present as foci and small arcs that colocalize with the cell envelope (white signal) and there were some foci in the center of the cell (Figure 7A top row). The CcmA-HaloTag signal closely resembled what we saw when we visualized CcmA-FLAG by immunofluorescence in previous work (Taylor *et al.*, 2020). In cells lacking *csd6*, we found that CcmA-HaloTag signal is present at the cell envelope and there are some foci in the center of cells (Figure 7A second row). In cells lacking *csd7*, cells are slightly curved and CcmA-HaloTag signal colocalizes with the cell envelope, however there are also some foci in the center of the cell (Figure 7A third row). In cells lacking *csd5*, there appears to be more CcmA-HaloTag signal in the center of cells than associated with the cell envelope (Figure 7A fourth row). In cells lacking both *csd5* and *csd7*, we found that the cell shape resembles a Δ*csd7* mutant, however, there appears to be more CcmA-HaloTag signal in the center of the cells than in the Δ*csd7* mutant, similar to the Δ*csd5* mutant (Figure 7A bottom row).

To quantify how much CcmA-HaloTag was located near the cell envelope as compared to the amount of CcmA-HaloTag found in the center of the cells, we developed

a method to measure the amount of CcmA-HaloTag signal that colocalized with the cell surface as we computationally generated sequential cell surface shells with smaller or larger diameters (Figure 7B and Expanded View Figure 4C-D). In both a WT and Δ*csd5* cell the WGA signal peaks at X=0 nm where the surface of the cell is. As we computationally shrink the surface of interest (X decreases), we observe the relative concentration of CcmA-HaloTag with respect to the position of the cell surface. In WT cells, CcmA-HaloTag signal peaks near -50 nm from the cell surface and declines further to the inside of the cell. In contrast, in a Δ*csd5* cell, the HaloTag-CcmA signal peaks near -100 nm from the cell surface and continues to be high even as the surface of interest approaches center of the cell (approximately -300 nm), indicating that more CcmA-HaloTag signal is found near the center of the cell in Δ*csd5* cells than in WT cells. When we performed the same analysis on the entire populations of cells (292 WT and 326 Δ*csd5*), we found that while the overall trends were the same as when we analyzed individual cells, there was a lot of variability in the WT cell population. The variability of the WT population is because many WT cells have both a population of CcmA-HaloTag at the cell envelope (peak at -50 nm) and in the center of the cell that causes a broader left tail in the population level data (Expanded View figure 4C-D). In contrast, the Δ*csd5* population level signal peak is broader and shifted towards the center of the cell (-80 nm). Thus, Csd5 is required for CcmA to localize to the cell envelope.

To identify where CcmA-HaloTag singal that is at the cell surface is in relation to cell curvature, we calculated the Gaussian curvature values of all cell surfaces represented in the populations. WT cells (which are helical) have a larger range of Gaussian curvature values on their cell surfaces (Figure 7 C-D) compared to all other

shape mutants. Interestingly, although all shape mutants are not helical, they do display different surface Gaussian curvature distributions and Δ*csd7* and Δ*csd5/7* populations look nearly identical, suggesting that Δ*csd5/7* double mutants resemble the shape of a Δ*csd7* mutant.

In WT cells, CcmA-HaloTag is enriched at the major helical axis (Gaussian curvature value of 5 ±1 μm^{-2} (Taylor *et al.*, 2020)); enrichment peaks at +3.35 μm^{-2} to +5.31 μm^{-2} Gaussian curvature and is depleted at Gaussian curvature values lower than +0.97 μm^{-2} and higher than +6.67 μm^{-2}. These data are consistent previous experiments where CcmA-FLAG was detected by immunofluorescence (Taylor *et al.*, 2020). In contrast, in all other strains, CcmA-HaloTag is depleted at regions of Gaussian curvature where CcmA-Halotag is enriched in WT cells (+3.35 μm^{-2} to +5.31 μm^{-2}) although those Gaussian curvature values are still present in all cell-shape-mutant populations (Figure 7 E-F). In Δ*csd6* and Δ*csd7* mutants, CcmA-HaloTag is enriched at negative Gaussian curvature values. In Δ*csd6* mutants, enrichment peaks at and continues to be enriched at all values lower than +0.11 μm^{-2} Gaussian curvature (to -4 μm^{-2} Gaussian curvature). In Δ*csd7* mutants, CcmA-HaloTag enrichment peaks at +0.15 μm^{-2} and is enriched at all values below +0.15 μm^{-2} (to -5.4 μm^{-2} Gaussian curvature), (Figure 7 E). In contrast to Δ*csd6* and Δ*csd7* mutants, in Δ*csd5* mutants, CcmA-HaloTag is depleted at negative Gaussian curvature values (Figure 7 F). Interestingly, in a Δ*csd5/7* double mutant, the CcmA-HaloTag enrichment pattern mirrors the Δ*csd5* mutant enrichment pattern. In Δ*csd5* mutants CcmA-HaloTag is enriched at Gaussian curvature values from -1.18 μm^{-2} to +2.5 μm^{-2} and has a peak enrichment at +0.68 μm^{-2}, CcmA-HaloTag is depleted at all other values of Gaussian curvature. In a Δ*csd5/7* double mutant CcmA-HaloTag is

enriched at Gaussian curvatures of -0.99 μm^{-2} to +3.46 μm^{-2} and peaks at +0.85 μm^{-2}, CcmA-HaloTag is depleted at all other values of Gaussian curvature. Suggesting that when helical cell shape is disrupted but Csd5 is present (in a Δ*csd6* or Δ*csd7* strain), CcmA localizes to regions of negative Gaussian curvature instead of the major helical axis and that Csd5, not Csd7 modulates CcmA localization.

Discussion

The helical cell shape of *H. pylori* is important for its ability to colonize the stomach (Martinez *et al.*, 2018; Montecucco & Rappuoli, 2001; Sycuro *et al.*, 2012; Yang *et al.*, 2019) and the mechanisms that control helical cell shape are still under active investigation. The PG sacculus is what ultimately controls the shape of bacterial cells and it has been hypothesized that modification of PG crosslinking generates curvature and twist of the sacculus (Huang *et al*, 2008; Sycuro *et al.*, 2010). In *H. pylori*, when the cytoplasmic bactofilin CcmA is lost, cells lose their helical shape and the PG muropeptide composition is altered (Sycuro *et al.*, 2010). But, how the cytoplasmic bactofilin CcmA impacts the PG sacculus in the periplasm was unclear. Recently, our group identified that the C-terminal bacterial SH3 domain of Csd5 directly interacts with PG in the periplasm, while its N-terminal domain interacts with CcmA in the cytoplasm (Blair *et al.*, 2018). In a separate study our group identified that CcmA also interacts with Csd7 (although the interaction appears to be weaker or potentially indirect), and Csd7 stabilizes the PG-hydrolase Csd1 and the scaffold protein Csd2. Interestingly, Δ*csd1*, Δ*csd2*, Δ*csd7*, and Δ*ccmA* mutants all share the same curved rod phenotype and PG muropeptide composition, suggesting that CcmA may regulate Csd1 activity, however a mechanism

linking CcmA and Csd1 was unclear (Sycuro *et al.*, 2010; Yang *et al.*, 2019). Additionally, we had identified that both CcmA and probes that report on PG synthesis are enriched at the major helical axis, suggesting that CcmA localization and PG synthesis are correlated spatially (Taylor *et al.*, 2020). In this study, we identified several new mechanisms that clarify how CcmA regulates the helical cell shape of *H. pylori* by modulating interactions with binding partners Csd5 and Csd7.

First, we identified that the N-terminal region of CcmA and the bactofilin domain are required for helical cell shape, but that the C-terminal region was not required. Next, in co-immunoprecipitation experiments, we found that the bactofilin domain of CcmA interacts with Csd5 and Csd7 and the N-terminal region inhibits the bactofilin domain from interacting with Csd7. When the N-terminal region of CcmA is removed, the bactofilin domain of CcmA binds to Csd7, destabilizing the Csd7-Csd1 complex and leading to Csd1 degradation, providing the first potential mechanism by which CcmA regulates Csd1.

Next, we identified that when other cell-shape-determining genes are deleted, CcmA can no longer localize to the major helical axis of the cell (Gaussian curvature value of 5 ±1 μm^{-2} (Taylor *et al.*, 2020)) suggesting that CcmA is directed to its preferred location by a binding partner and is not capable of localizing to or sensing cell envelope curvature on its own. Loss of Csd7 or Csd6 individually generate the same CcmA enrichment pattern, CcmA to localizes to regions of negative Gaussian curvature. In comparison, loss of Csd5 or loss of both Csd5 and Csd7 together causes substantially less CcmA to localize to the cell envelope than in all other conditions. The CcmA signal that does co-localize with the cell envelope in Δ*csd5* and Δ*csd5/7* cells is enriched near zero Gaussian

curvature, and is depleted at all other Gaussian curvature values. These data suggest that Csd5 recruits CcmA to the cell envelope. If helical cell shape is disrupted (due to loss of another cell shape protein) while Csd5 is still present, Csd5 directs CcmA to regions of negative Gaussian curvature. Additionally, the finding that CcmA localization phenotypes are the same in a Δ*csd5* mutant and a Δ*csd5/7* double mutant suggest that Csd7 does not control CcmA localization, bolstering the previous finding that Csd7 and CcmA only interact at low levels in WT cells (Yang *et al.*, 2019).

Using what we have learned in this study, we can revise our model of the protein complex that patterns the helical shape of *H. pylori* cells. CcmA's bactofilin domain interacts with the cytoplasmic N-terminal region of the transmembrane protein Csd5 which likely directs CcmA to the cell envelope. Csd5 brings MurF and other potential PG synthesis machinery to the same region of the cell envelope for new PG to be inserted into the cell wall (Figure 8). CcmA's N-terminal region inhibits interaction of CcmA's bactofilin domain with Csd7, allowing Csd7 to stabilize Csd1. Thus, CcmA regulates Csd1 activity (cleaving tetra-pentapeptide crosslinks) spatially or temporally in relation to Csd5 and MurF to organize PG modification and insertion. Our work raises the question of whether Csd5 senses curvature. Alternatively, the C-terminal SH3 domain of Csd5 can bind to PG directly (Blair *et al.*, 2018) and may sense a particular curvature or structure of the cell wall.

In addition to understanding how the helical cell shape of *H. pylori* is controlled, this study provides information about how CcmA and potentially other bactofilins function. Modeling combined with circular dichroism data suggest that the bactofilin domain is a β-helix and the two short terminal regions are largely unstructured. Additionally, circular

dichroism data suggest that two previously studied CcmA point mutants that cause loss of function are unfolded. The I55 and L110 residues are homologous to residues mutated by Vasa and colleagues in BacA (V75 and F130 in BacA) and are predicted to reside in the interior of the hydrophobic core of the proteins and mutating these residues destabilizes the proteins likely through the hydrophobic effect (Taylor *et al.*, 2020; Vasa *et al.*, 2015). We also identified that the bactofilin domain is capable of polymerizing on its own, the N-terminal region promotes lateral interactions between filaments, and the N- and C- terminal regions are both necessary for lattice formation. These data correlate with what has been previously reported in the literature; in the bactofilin Ttbac from *T. thermophilus* loss of the N-terminal region (residues 1-10 in Ttbac) generated smaller, more ordered bundles of filaments (Deng *et al.*, 2019), and it has been previously reported that purified Δ*CT* CcmA from *H. pylori* does not form lattice structures (Holtrup *et al.*, 2019).

In this study, we identified several putative functional motifs. The N-terminal region (amino acids 1-18) is important for patterning helical cell shape and regulates interactions with Csd7, suggesting that the N-terminal region is a functional motif. Our data also suggest that amino acids 13-17 in the N-terminal region of CcmA promote lateral interactions between filaments *in vitro* and may be another functional motif. However, in CcmA, the putative membrane binding motif (amino acids 3-12) did not show any clear function. Additionally, the C-terminal region of CcmA is not required for any of the cellular phenotypes assayed (cell shape, Csd5 or Csd7 interactions, Csd1 stabilization).

Bactofilins are commonly found as part of complexes in other bacteria and help spatially organize cells to regulate where certain functions occur (Sichel & Salama, 2020;

Surovtsev & Jacobs-Wagner, 2018). Our findings regarding how CcmA functions within a complex in *H. pylori* may provide insight into how bactofilins operate within complexes in other bacterial species. Mechanisms similar to how CcmA functions in *H. pylori* have been reported in other systems; in *A. biprostecum* a PG hydrolase, SpmX, directs the bactofilin BacA to the site of stalk synthesis, then BacA organizes the rest of the complex (Caccamo *et al.*, 2020) to control stalk morphogenesis. Interestingly, the genomic arrangement of *csd1* (an M23 metallopeptidase) and *CcmA* overlapping is conserved in several other curved and helical species of Epsilonproteobacteria and Gammaproteobacteria (Billini *et al.*, 2019; Caccamo *et al.*, 2020; Sycuro *et al.*, 2010), and has been reported in a spirochete (Jackson *et al.*, 2018), suggesting that bactofilins may regulate M23 metallopeptidases to promote PG remodeling at specific regions of the cell envelope to control cell shape and morphogenesis of other morphological features. Our work is the first to suggest a mechanism of how a bactofilin can regulate a PG hydrolase indirectly through an integral membrane protein and protein stability.

Materials and Methods

Bacterial strains and growth

Strains used in this work, as well as primers and plasmids used in strain construction are available in the appendix. *H. pylori* was grown in Brucella Broth (BD) supplemented with 10% heat-inactivated fetal bovine serum (Cytiva Hyclone) without antimicrobials or on

horse blood agar plates with microbials as described (Sycuro *et al.*, 2010). For resistance marker selection, horse blood agar plates were supplemented with 15 µg/ml chloramphenicol, 25 µg/ml kanamycin, or 60 mg/ml sucrose. *H. pylori* strains were grown at 37 °C under micro-aerobic conditions in a tri-gas incubator (10% CO_2, 10% O_2, and 80% N_2). For plasmid selection and maintenance in *E. coli,* cultures were grown in Lysogeny broth (LB) or on LB-agar at 37 °C supplemented with 100 µg/mL ampicillin or 25 µg/ml Kanamycin.

Protein structure prediction

Swiss-Model was used to identify the boundaries between the bactofilin domain and the terminal regions of CcmA. The primary amino acid sequence of CcmA from the *H. pylori* G27 genome (GenBank: CP001173.1) was submitted to Swiss-Model (https://swissmodel.expasy.org/ (Waterhouse *et al.*, 2018)) where the structure of BacA from *C. crescentus* (Vasa *et al.*, 2015) was used to model CcmA. RoseTTAFold was used to predict the structure of CcmA; the same primary amino acid sequence of CcmA was submitted to the Robetta protein prediction service (https://robetta.bakerlab.org/ (Baek *et al.*, 2021)). Models generated in RoseTTAFold were modified in Pymol (The PyMOL Molecular Graphics System, Version 2.4.2 Schrödinger, LLC.).

Western blotting

Whole cell extracts of *H. pylori* were prepared by harvesting 1.0 optical density at 600 nm (OD_{600}) of log phase liquid culture (0.3-0.7 OD_{600}) by centrifugation for 2 minutes. Then, bacteria were resuspended to a concentration of 10 OD_{600} per ml with 2x protein sample

buffer (0.1 M Tris-HCl, 4% SDS, 0.2% bromophenol blue, 20% glycerol) with or without 5% β-mercaptoethanol (BME). Samples were loaded onto Mini-PROTEAN TGX 4-15% polyacrylamide gels (Bio-Rad) and transferred onto polyvinylidene difluoride (PVDF) membranes using the Trans-Blot TurboTransfer System (Bio-Rad) system. Membranes were either stained with 0.1% Ponceu S solution in 5% acetic acid (Sigma) first, or immediately blocked for 2 hours at room temperature in 5% non-fat milk in tris-buffered saline containing 0.05% tween-20 (TBS-T) then incubated either overnight at 4 °C or at room temperature for 1 hour with primary antibodies, 1:10,000 for α-CcmA (Blair et al., 2018), 1:5,000 for α-FLAG (M2, Sigma), 1:10,000 for α-Csd1 (Yang *et al.*, 2019), or 1:20,000 for α-cag3 (Pinto-Santini & Salama, 2009). Then washed 5 times with TBS-T over a 30-minute period, incubated with secondary antibodies for 1 hour at room temperature at 1:20,000 with appropriate horseradish peroxidase-conjugated α-immunoglobulin antibodies (α-rabbit for CcmA Csd1, or Cag3; α-mouse for FLAG, Santa Cruz Biotechnology), then washed 5 times with TBS-T over a 30-minute period. Proteins were detected using a chemiluminescent substrate according to manufacturer's instructions (Pierce ECL substrate for standard western blotting or Immobilon Western HRP substrate (Millipore) for western blotting following co-immunoprecipitation experiments) and imaged directly with the Bio-Rad gel documentation system.

Phase contrast microscopy and quantitative morphology analysis

Phase contrast microscopy and image analysis was performed as previously described (Sycuro *et al.*, 2010). Briefly, cells were grown in liquid culture to mid-log phase (0.3-0.7 OD_{600}), centrifuged, and resuspended in 4% paraformaldehyde (PFA) in phosphate-

buffered saline (PBS) and mounted on glass slides. Cells were imaged with a Nikon TE 200 microscope equipped with a 100X oil immersion lens objective and Photometrics CoolSNAP HQ charge-coupled-device camera. Images were thresholded with FIJI (Schindelin *et al*, 2012) and CellTool software (Pincus & Theriot, 2007) was used to measure both side curvature and central axis length.

Protein purification

Purification of 6-his CcmA was performed exactly as described previously (Taylor *et al.*, 2020). *E. coli* strains used to recombinantly express CcmA were: pKB62A in BL21 DE3, pSS15A in BL21 DE3, pSS16A in BL21 DE3, pSS17A in BL21 DE3, pSS18B in BL21 DE3, pSS19A in BL21 DE3, pKB69H in BL21 DE3, and pKB72D in BL21 DE3 and are described in detail in the appendix.

Circular dichroism

After purification of 6-his CcmA, samples were dialyzed against 10 mM CAPS pH 11 at a volume of 1:10,000 for 24 hours, then the buffer was changed, and dialysis continued for another 24 hours. After dialysis was complete, samples were normalized to 0.5 mg/ml. CD spectra were collected from 180-260 nm while holding the temperature constant with a Jasco J-815 Circular Dichroism Spectropolarimeter.

Negative stain and Transmission Electron Microscopy (TEM)

After purification of 6-his CcmA samples were dialyzed against 25 mM Tris pH 8 for 24 hours. Samples were then normalized to 1 mg/ml and placed on carbon-coated grids after

glow-discharging. Samples were fixed in ½ X Karnovsky's fixative and washed with 0.1 M Cacodylate buffer and water, then stained with Nano-W (Nanoprobes) for 60 seconds, wicked, then stained for another 60 seconds. Images were acquired on a kV ThermoFisher Talos 120C LaB_6 microscope equipped with a Ceta Camera using Leginon software (Suloway *et al*, 2005). The width of bundles and filaments were measured using FIJI (Schindelin *et al.*, 2012).

Co-immunoprecipitation experiments

Co-immunoprecipitation experiments were performed as previously described in Blair *et al.,* 2018 and Yang *et al.,* 2019 with slight variations. *H. pylori* expressing FLAG tags fused to either Csd5 or Csd7 were grown to mid-log phase in liquid culture and 15 OD_{600} were harvested by centrifugation at 10,000 RPM for 10 minutes at 4 °C. Cells pellets were resuspended in 1.8 ml of cold lysis buffer (20 mM tris pH 8, 150 mM NaCl, 2% glycerol, 1% Triton X-100 and EDTA-free protease inhibitor (Pierce)). The cells were sonicated at 10% power for 10 second intervals with a microtip (Sonic Dismembrator Model 500, Branson) until visibly cleared, then centrifuged at 20,000 RCF for 30 minutes at 4 °C. The soluble fraction was then incubated with 40 µl beads (α-FLAG M2 agarose beads (Sigma) or α-VSV-G agarose beads (Sigma) equilibrated in wash buffer (20 mM tris pH 8, 150 mM NaCl, 2% glycerol, 0.1% Triton X-100) for 90 minutes at 4 °C. The beads were then washed four times in 10 ml cold wash buffer, samples were centrifuged at 2000 RPM for 2 minutes between washes. Beads were then boiled in 45 µl 2x sample buffer without BME for 10 minutes and subjected to western blotting.

Labeling with fluorescent WGA and HaloTag ligands

H. pylori expressing CcmA-HaloTag were grown to mid-log phase and fixed with 4% PFA for 45 minutes at room temperature. After fixing, bacteria were permeabilized for 1 hour at room temperature with PBS + 0.05% Triton X-100. Bacteria were then resuspended in PBS and centrifuged onto #1.5 coverslips. Next, coverslips were incubated on a droplet of PBS containing 30 µg/ml af488-conjucated WGA (Invitrogen) and 4 µM JF-549 (Promega) for 30 minutes at room temperature. Coverslips were washed four times (10 minutes each) by placing on fresh droplets of PBS + 0.1% Tween-20, then mounted on glass slides with ProLong Diamond Antifade Mountant (Invitrogen).

3D Structured Illumination Microscopy

3D structured illumination microscopy (SIM) was performed on a DeltaVIsion OMX SR equipped with PCO scientific CMOS cameras, 488 nm and 568 nm lasers, and an Olympus 60X/1.42 U PLAN APO oil objective with oil matched for the sample refractive index. 512 x 512 pixel Z-stack images were acquired with 125 nm spacing and 3 µm total thickness. Figures were generated by changing channel colors, adjusting brightness and contrast in FIJI, brightness and contrast settings were maintained across the entire image (Schindelin *et al.*, 2012). Figures were assembled in Adobe Illustrator.

3D reconstructions and curvature enrichment analysis

3D reconstructions were generated, and curvature CcmA enrichment analysis was preformed exactly as described in Taylor *et al.,* 2020 using existing software (Bratton *et al.*, 2019; Bratton *et al*, 2018). Briefly, 3D SIM Z-stack images were used to generate a

3D triangular meshwork surface with roughly 30 nm precision from the WGA channel. After generating the 3D triangular meshwork, the Gaussian curvature was calculated at every location on the surface of the cell and we performed curvature enrichment analysis to identify which GC values CcmA signal was associated with where uniform signal=1. Because the absolute amount of CcmA signal can differ between cells and because the illumination throughout the field is non-uniform, we set the average CcmA signal on each cell as one. Then we measured each cell's curvature dependent CcmA signal intensity relative to one, normalized by the amount of the curvature present on that individual cell surface.

Analysis of intensity of CcmA-HaloTag signal at cell surface and within cells

A custom Matlab script was used to compute the relative intensity of CcmA-HaloTag signal at the cell surface and at surfaces generated by shrinking the surface of interest toward the centerline of the cell (negative offsets) or increasing the surface away from the centerline (positive offsets). For each of these shells, or surface offsets, we calculated the average WGA signal and the average CcmA-HaloTag signal. To account for errors in spatial alignment between the two color channels, before calculating the intensity at each shell, we performed a rigid body alignment procedure to maximize the intensity of the signal contained within the nominal reconstructed surface (0 nm offset). Consistent with the fact that we utilized the WGA channel for shape reconstructions, this alignment algorithm returned offsets of less than one pixel for the WGA channel. The CcmA-HaloTag channel showed more variability in the offsets, sometimes requiring an offset of almost 200 nm along the focal direction, consistent with small, wavelength dependent

variations in focal position. After calculating the average intensity at each subshell, or resized surface, we normalized the highest concentration to 1 before averaging across all the cells in our sample.

Acknowledgements

This research was supported by the US National Institute of Heath (NIH) grants F31 AI152331 (SRS), T32 GM95421 (SRS), R01 AI136946 (NRS). As well as the GO-MAP Graduate Opportunity Program Research Assistantship award (GOP Award) (SRS) and the VUMC Discovery Scholars in Health and Medicine Program (BPB). This research was supported by the Genomics and Cellular Imaging and Electron Microscopy shared resources of the Fred Hutch/University of Washington Cancer Consortium (P30 CA015704). The opinions, findings, and conclusions or recommendations expressed in this material contents are solely the responsibility of the authors and do not necessarily represent the official views of the NIH.

We would like to thank Joseph Stembel (University of Washington) for construction of strains JS02 and JS09, Jennifer Taylor (University of Washington) for helpful advice and training, Ethan Garner (Harvard) for helpful discussion, James McDermott for thoughtful discussion and review of this manuscript, David Baker and Justin Decarreau (University of Washington), and the support of the Audacious Project at the Institute for Protein Design for use of the DeltaVision OMX microscope, Roland Strong and Barry Stoddard (Fred Hutchinson Cancer Center) for use of the Circular Dichroism Spectropolarimeter, and Caleigh Azumaya (Fred Hutchinson Cancer Center) for assistance with the Talos microscope.

Data Availability

The datasets and computer code produced in this study will be available soon at the following locations:

- Matlab scripts and documentation: https://github.com/PrincetonUniversity/shae-cellshape-public.
- Imaging datasets: https://www.ebi.ac.uk/bioimage-archive/

Author contributions

Conception and design of the study (SRS, NRS), acquisition of data (SRS), analysis and interpretation of data (SRS, NRS, BPB), writing the manuscript (SRS, NRS).

Conflict of interest

The authors have no conflicts of interest to report.

References

Baek M, DiMaio F, Anishchenko I, Dauparas J, Ovchinnikov S, Lee GR, Wang J, Cong Q, Kinch LN, Schaeffer RD *et al* (2021) Accurate prediction of protein structures and interactions using a three-track neural network. *Science* 373: 871-876

Billini M, Biboy J, Kuhn J, Vollmer W, Thanbichler M (2019) A specialized MreB-dependent cell wall biosynthetic complex mediates the formation of stalk-specific peptidoglycan in Caulobacter crescentus. *PLoS Genet* 15: e1007897

Blair KM, Mears KS, Taylor JA, Fero J, Jones LA, Gafken PR, Whitney JC, Salama NR (2018) The Helicobacter pylori cell shape promoting protein Csd5 interacts with the cell wall, MurF, and the bacterial cytoskeleton. *Mol Microbiol* 110: 114-127

Bratton BP, Barton B, Morgenstein RM (2019) Three-dimensional Imaging of Bacterial Cells for Accurate Cellular Representations and Precise Protein Localization. *J Vis Exp*

Bratton BP, Shaevitz JW, Gitai Z, Morgenstein RM (2018) MreB polymers and curvature localization are enhanced by RodZ and predict E. coli's cylindrical uniformity. *Nat Commun* 9: 2797

Brockett MR, Lee J, Cox JV, Liechti GW, Ouellette SP (2021) A Dynamic, Ring-Forming Bactofilin Critical for Maintaining Cell Size in the Obligate Intracellular Bacterium Chlamydia trachomatis. *Infect Immun* 89: e0020321

Bulyha I, Lindow S, Lin L, Bolte K, Wuichet K, Kahnt J, van der Does C, Thanbichler M, Sogaard-Andersen L (2013) Two small GTPases act in concert with the bactofilin cytoskeleton to regulate dynamic bacterial cell polarity. *Dev Cell* 25: 119-131

Caccamo PD, Jacq M, VanNieuwenhze MS, Brun YV (2020) A Division of Labor in the Recruitment and Topological Organization of a Bacterial Morphogenic Complex. *Curr Biol* 30: 3908-3922 e3904

de Martel C, Georges D, Bray F, Ferlay J, Clifford GM (2020) Global burden of cancer attributable to infections in 2018: a worldwide incidence analysis. *The Lancet Global Health* 8: e180-e190

Deng X, Gonzalez Llamazares A, Wagstaff JM, Hale VL, Cannone G, McLaughlin SH, Kureisaite-Ciziene D, Lowe J (2019) The structure of bactofilin filaments reveals their mode of membrane binding and lack of polarity. *Nat Microbiol* 4: 2357-2368

El Andari J, Altegoer F, Bange G, Graumann PL (2015) Bacillus subtilis Bactofilins Are Essential for Flagellar Hook- and Filament Assembly and Dynamically Localize into Structures of Less than 100 nm Diameter underneath the Cell Membrane. *PLoS One* 10: e0141546

Greenfield NJ (2006) Using circular dichroism spectra to estimate protein secondary structure. *Nat Protoc* 1: 2876-2890

Hay NA, Tipper DJ, Gygi D, Hughes C (1999) A Novel Membrane Protein Influencing Cell Shape and Multicellular Swarming of Proteus mirabilis. *Journal of Bacteriology* 181: 2008-2016

Holtrup S, Heimerl T, Linne U, Altegoer F, Noll F, Waidner B (2019) Biochemical characterization of the Helicobacter pylori bactofilin-homolog HP1542. *PLoS One* 14: e0218474

Hooi JKY, Lai WY, Ng WK, Suen MMY, Underwood FE, Tanyingoh D, Malfertheiner P, Graham DY, Wong VWS, Wu JCY *et al* (2017) Global Prevalence of Helicobacter pylori Infection: Systematic Review and Meta-Analysis. *Gastroenterology* 153: 420-429

Hrast M, Turk S, Sosic I, Knez D, Randall CP, Barreteau H, Contreras-Martel C, Dessen A, O'Neill AJ, Mengin-Lecreulx D *et al* (2013) Structure-activity relationships of new

cyanothiophene inhibitors of the essential peptidoglycan biosynthesis enzyme MurF. *Eur J Med Chem* 66: 32-45

Huang KC, Mukhopadhyay R, Wen B, Gitai Z, Wingreen NS (2008) Cell shape and cell-wall organization in Gram-negative bacteria. *Proc Natl Acad Sci U S A* 105: 19282-19287

Jackson KM, Schwartz C, Wachter J, Rosa PA, Stewart PE (2018) A widely conserved bacterial cytoskeletal component influences unique helical shape and motility of the spirochete Leptospira biflexa. *Mol Microbiol* 108: 77-89

Koch MK, McHugh CA, Hoiczyk E (2011) BacM, an N-terminally processed bactofilin of Myxococcus xanthus, is crucial for proper cell shape. *Mol Microbiol* 80: 1031-1051

Kuhn J, Briegel A, Morschel E, Kahnt J, Leser K, Wick S, Jensen GJ, Thanbichler M (2010) Bactofilins, a ubiquitous class of cytoskeletal proteins mediating polar localization of a cell wall synthase in Caulobacter crescentus. *EMBO J* 29: 327-339

Lin L, Osorio Valeriano M, Harms A, Sogaard-Andersen L, Thanbichler M (2017) Bactofilin-mediated organization of the ParABS chromosome segregation system in Myxococcus xanthus. *Nat Commun* 8: 1817

Martinez LE, O'Brien VP, Leverich C, Knoblaugh SE, Salama NR (2018) Non-helical Helicobacter pylori show altered gland colonization and elicit less gastric pathology during chronic infection. *bioRxiv*: 505107

Montecucco C, Rappuoli R (2001) Living dangerously: how Helicobacter pylori survives in the human stomach. *Nat Rev Mol Cell Biol* 2: 457-466

Osorio-Valeriano M, Altegoer F, Steinchen W, Urban S, Liu Y, Bange G, Thanbichler M (2019) ParB-type DNA Segregation Proteins Are CTP-Dependent Molecular Switches. *Cell* 179: 1512-1524 e1515

Pincus Z, Theriot JA (2007) Comparison of quantitative methods for cell-shape analysis. *J Microsc* 227: 140-156

Pinto-Santini DM, Salama NR (2009) Cag3 is a novel essential component of the Helicobacter pylori Cag type IV secretion system outer membrane subcomplex. *J Bacteriol* 191: 7343-7352

Schindelin J, Arganda-Carreras I, Frise E, Kaynig V, Longair M, Pietzsch T, Preibisch S, Rueden C, Saalfeld S, Schmid B *et al* (2012) Fiji: an open-source platform for biological-image analysis. *Nat Methods* 9: 676-682

Sichel SR, Salama NR (2020) Bacterial Cell Biology: It Takes Two to Tango. *Curr Biol* 30: R1258-R1260

Smeets LC, Bijlsma JJ, Boomkens SY, Vandenbroucke-Grauls CM, Kusters JG (2000) comH, a novel gene essential for natural transformation of Helicobacter pylori. *J Bacteriol* 182: 3948-3954

Suloway C, Pulokas J, Fellmann D, Cheng A, Guerra F, Quispe J, Stagg S, Potter CS, Carragher B (2005) Automated molecular microscopy: the new Leginon system. *J Struct Biol* 151: 41-60

Surovtsev IV, Jacobs-Wagner C (2018) Subcellular Organization: A Critical Feature of Bacterial Cell Replication. *Cell* 172: 1271-1293

Sycuro LK, Pincus Z, Gutierrez KD, Biboy J, Stern CA, Vollmer W, Salama NR (2010) Peptidoglycan crosslinking relaxation promotes Helicobacter pylori's helical shape and stomach colonization. *Cell* 141: 822-833

Sycuro LK, Rule CS, Petersen TW, Wyckoff TJ, Sessler T, Nagarkar DB, Khalid F, Pincus Z, Biboy J, Vollmer W *et al* (2013) Flow cytometry-based enrichment for cell shape mutants identifies multiple genes that influence Helicobacter pylori morphology. *Mol Microbiol* 90: 869-883

Sycuro LK, Wyckoff TJ, Biboy J, Born P, Pincus Z, Vollmer W, Salama NR (2012) Multiple peptidoglycan modification networks modulate Helicobacter pylori's cell shape, motility, and colonization potential. *PLoS Pathog* 8: e1002603

Taylor JA, Bratton BP, Sichel SR, Blair KM, Jacobs HM, DeMeester KE, Kuru E, Gray J, Biboy J, VanNieuwenhze MS *et al* (2020) Distinct cytoskeletal proteins define zones of enhanced cell wall synthesis in Helicobacter pylori. *Elife* 9

Vasa S, Lin L, Shi C, Habenstein B, Riedel D, Kuhn J, Thanbichler M, Lange A (2015) beta-Helical architecture of cytoskeletal bactofilin filaments revealed by solid-state NMR. *Proc Natl Acad Sci U S A* 112: E127-136

Waterhouse A, Bertoni M, Bienert S, Studer G, Tauriello G, Gumienny R, Heer FT, de Beer TAP, Rempfer C, Bordoli L *et al* (2018) SWISS-MODEL: homology modelling of protein structures and complexes. *Nucleic Acids Res* 46: W296-W303

Yang DC, Blair KM, Taylor JA, Petersen TW, Sessler T, Tull CM, Leverich CK, Collar AL, Wyckoff TJ, Biboy J *et al* (2019) A Genome-Wide Helicobacter pylori Morphology Screen Uncovers a Membrane-Spanning Helical Cell Shape Complex. *Journal of Bacteriology* 201: e00724-00718

Figure legends

Figure 1- Predicted structure of CcmA. (A) Sequence alignment between BacA from *C. crescentus* and CcmA from *H. pylori* generated with SwissModel, gray boxes indicate β-strands formed in the bactofilin domain, the green box indicates the N-terminal region of CcmA and the pink box indicates the C-terminal region of CcmA. (B) Model of the bactofilin domain of CcmA generated by Robetta which forms a right-handed, 3-sided, triangular β-helix. (C) Five models of CcmA generated in Robetta displaying the bactofilin domain (gray), N-terminal region (green), and C-terminal region (pink).

Figure 2- *H. pylori* cells expressing various CcmA truncation mutants have different cell shapes. (A) Schematic of CcmA and truncation mutants. The N-terminal region (NT, green), bactofilin domain (BD, cyan), and C-terminal region (CT, pink) are indicated as well as the putative membrane binding motif (MM). (B) Western blot to detect CcmA in *H. pylori* strains expressing truncated versions of CcmA probed with α-CcmA polyclonal antibody, and α-Cag3 polyclonal antibody as a loading control. (C) Phase contrast images of *H. pylori* strains expressing truncated versions of CcmA diagramed in panel A, scalebars = 1 μm. (D) Histogram displaying the side curvature of *H. pylori* strains expressing truncated versions of CcmA (WT n= 476 cells, Δ*ccmA* n= 397 cells, Δ*N* n=275

cells, Δ*MM* n= 391 cells, Δ13-17 n=361 cells, Δ*CT* n= 263 cells, BD n=315 cells). Data are representative of two independent biological replicates. Strains used: SSH51A, SSH53A, SSH55A, SSH54A, SSH67A, SSH56B, and SSH57A.

Figure 3- Circular dichroism spectra of purified 6-his CcmA suggests CcmA is composed of predominantly β-sheets. (A) Circular dichroism spectra of WT and truncated versions of CcmA at room temperature (20 ºC), WT (black), Δ*NT* (green), Δ*CT* (pink), and BD (cyan). (B) Circular dichroism spectra of WT CcmA at room temperature (20 ºC, black), melted (95 ºC, dotted line), and two point mutants (I55A, red and L110S, burgundy).

Figure 4- The bactofilin domain of CcmA is sufficient for *in vitro* polymerization while the terminal regions promote lateral polymer interactions. (A-F) TEM of negative stained, purified CcmA, scalebars = 500 nm. White boxes indicate region of micrograph that is enlarged in panel to the right of original. White arrows indicate bundles of CcmA, black arrows indicate lattice structures, red arrow indicates two bundles wrapping around each other. Data are representative of two independent biological replicates. (G) Box and whiskers plot displaying width of purified CcmA bundles and filaments. Median, min, max, 25th percentile, and 75th percentile are displayed. One-way ANOVA, Dunnett's multiple comparisons test. ns P>0.5, *** P≤0.001, **** P ≤0.0001. WT n=24, Δ*NT* n=29, Δ*MM* n=25, Δ*13-17* n=31, Δ*CT* n=24, BD n=32.

Figure 5 – The bactofilin domain interacts with Csd5 and Csd7, and the N-terminal region inhibits Csd7 binding to CcmA. Co-immunoprecipitation experiments to probe Csd5-2x-

FLAG-CcmA interactions (A) and Csd7-3x-FLAG-CcmA interactions (B) in *H. pylori* cells are shown. Top row: ponceau staining of input fractions. Second row: western blot probed with α-CcmA polyclonal antibody of input fractions. Third row: western blot probed with α-FLAG monoclonal antibody of immunoprecipitation (IP) fractions. Bottom row: western blot probed with α-CcmA polyclonal antibody of IP fractions. Data shown are representative of data from three independent biological replicates. Strains used: KHB157, LSH100, SSH59A, SSH58A, SSH68A, SSH60A, SSH65A, DCY71, SSH79A, SSH78A, SSH82, SSH80A, and SSH81B.

Figure 6- Csd1 expression is diminished in strains lacking the N-terminal region of CcmA. Western blot of whole cell extracts probed with α-Csd1 polyclonal antibody showing expression of Csd1 in CcmA truncation mutants, α-Cag3 polyclonal antibody was used as a loading control. Strains with "csd1^{c}" indicate a second copy of *csd1* was added at the *rdxA* locus. Data shown are representative of data from three independent biological replicates. Strains used: LSH100, LSH113, DCY26, SSH51A, SSH53A, SSH55A, SSH54A, SSH67A, SSH56B, and SSH57A.

Figure 7- Csd5 promotes CcmA cell envelope localization. (A) Maximum intensity projections (MIP) and frames from Z-stacks of *H. pylori* cells labeled with WGA to label the cell wall (magenta) and JF549 ligand to label CcmA-HaloTag (green). Green arrows indicated cytoplasmic CcmA-HaloTag. White arrows indicate CcmA-HaloTag signal that colocalizes with the cell envelope. Scalebars = 1 µm. (B) Representative plots displaying the relative concentration of HaloTag-CcmA and WGA signal from one WT and one Δ*csd5*

cell at the cell surface (X=0) and at computationally generated cell surfaces that are inside (X<0) and outside (X>0) of the cell surface. (C) Representative *H. pylori* cells from each population with Gaussian curvature values mapped on the cell surface. (D-E) Top, histogram of Gaussian curvature of cell surfaces of each population. Bottom, surface Gaussian curvature enrichment of relative concentration of CcmA signal in each population where 1=uniform concentration of CcmA. In panels C-F, WT n=292, Δ*csd6* n=264 cells, Δ*csd7* n=355, Δ*csd5* n=326, Δ*csd5/7* n=523. Strains used: SSH39B, SSH49A, SSH50A, JS09, and SSH70A.

Figure 8- Schematic depicting CcmA's role in the helical cell shape complex. (A) In WT cells, Csd5 recruits WT CcmA to the cell envelope via CcmA's bactofilin domain. The N-terminal region of CcmA inhibits interaction with Csd7, allowing Csd1 to function and excluding Csd1 from the CcmA-Csd5-MurF complex. (B) In cells expressing CcmA Δ*NT,* Csd5 recruits Δ*NT* CcmA to the cell envelope via CcmA's bactofilin domain. The bactofilin domain of CcmA binds to Csd7, inhibiting Csd7 from stabilizing Csd1. (C) When Csd5 is absent, CcmA cannot localize to the cell envelope, MurF is not directed to a particular location. OM = outer membrane, IM =inner membrane. This figure was created using Biorender.com.

<u>Expanded View Figure Legends</u>

Expanded View Figure 1- Robust CcmA detection with α-CcmA polyclonal antibody requires the C-terminus. 0.1 µg of purified protein was loaded into each lane. Top row:

Ponceau S staining of purified 6-his-CcmA. Bottom Row: western blot probed with polyclonal α-CcmA antibody, both images are of the same membrane.

Expanded View Figure 2- Purification of WT and mutant 6-his CcmA. (A) Coomassie-stained gel of induced, whole cell lysates of *E. coli*. (B) Coomassie-stained gel of the first elution after purification of 6-his CcmA with cobalt affinity resin.

Expanded View Figure 3- The C-terminus of CcmA-HaloTag is not required for interactions with Csd5. α-FLAG immunoprecipitation of strains expressing Csd5-FLAG and WT CcmA-HaloTag, CcmA Δ*CT*-HaloTag, or CcmA BD only -HaloTag. Top Row: Ponceau S staining of input fractions. Second row: western blot of inputs probed with α-HaloTag monoclonal antibody to detect CcmA-HaloTag, both top and second row are images of the same membrane. Third row: western blot of IP fractions probed with α-FLAG monoclonal antibody to detect Csd5-FLAG. Bottom row: western blot of IP fractions probed with α-HaloTag monoclonal antibody to detect CcmA-HaloTag. Strains used: SSH87A, SSH89A, and SSH97A

Expanded View Figure 4- Cell shape of CcmA-HaloTag strains. (A) Scatterplot of outlines of *H. pylori* cells derived from phase contrast images. (B) Histogram displaying side curvature of each population. WT (LSH100) n=116 cells, *ccmA::ccmA-Halotag* (SSH38A) n=133 cells, *ccmA::ccmA-HaloTag, rdxA::ccmA* (SSH39B) n=190 cells. (C-D) Plots displaying the relative concentration of HaloTag-CcmA and WGA signal at the cell surface (X=0) and at computationally generated cell surfaces that are inside (X<0) and outside

(X>0) of the cell surface. Populations of WT (C) and Δ*csd5* (D) cells from three independent experiments were pooled.

Figure 1

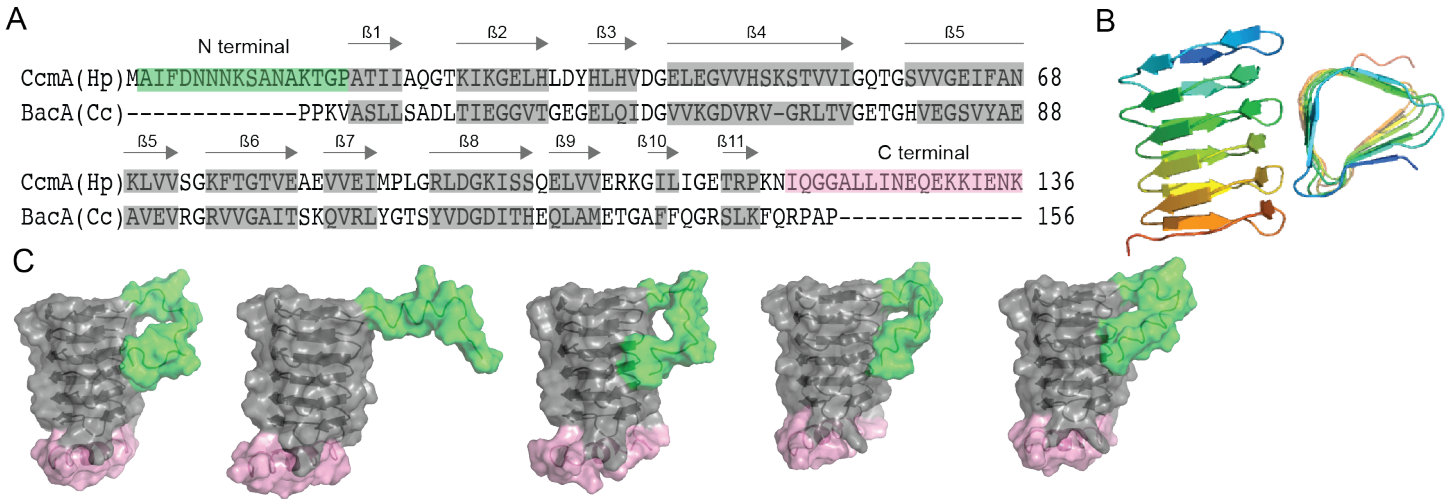
A
N terminal
ß1
ß2
ß3
ß4
ß5
CcmA(Hp)MAIFDNNNKSANAKTGPATIIAQGTKIKGELHLDYHLHVDGELEGVVHSKSTVVIGQTGSVVGEIFAN 68
BacA(Cc)----------PPKVASLLSADLTIEGGVTGEGELQIDGVVKGDVRV-GRLTVGETGHVEGSVYAE 88
ß5
ß6
ß7
ß8
ß9
ß10
ß11
C terminal
CcmA(Hp)KLVVSGKFTGTVEAEVVEIMPLGRLDGKISSQELVVERKGILIGETRPKNIQGGALLINEQEKKIENK 136
BacA(Cc)AVEVRGRVVGAITSKQVRLYGTSYVDGDITHEQLAMETGAFFQGRSLKFQRPAP---------- 156
B
C

Figure 2

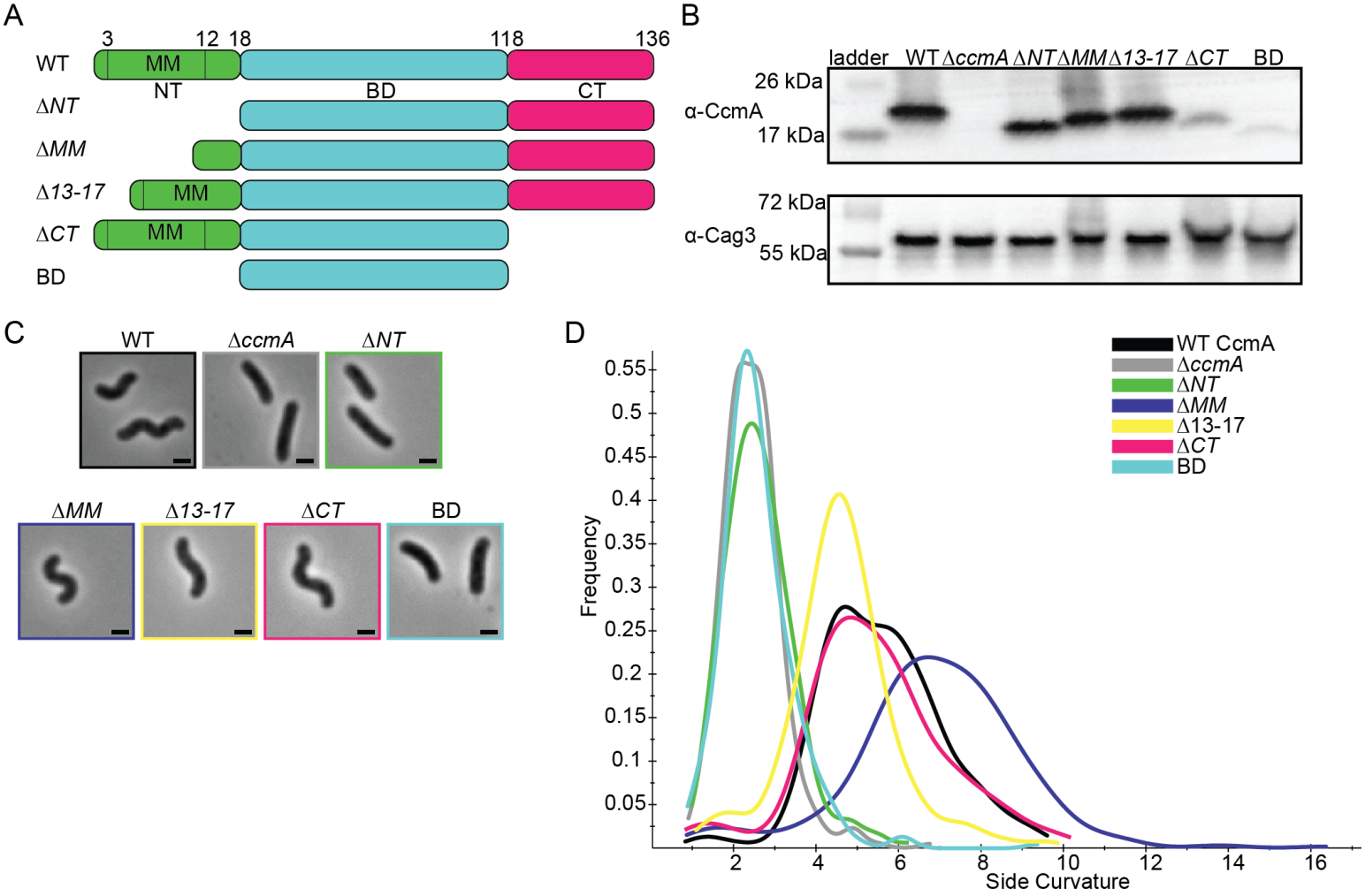
A
3
12
18
118
136
WT
MM
NT
BD
CT
ΔNT
ΔMM
Δ13-17
ΔCT
BD
B
ladder
WT
ΔccmA
ΔNT
ΔMM
Δ13-17
ΔCT
BD
26 kDa
α-CcmA
17 kDa
72 kDa
α-Cag3
55 kDa
C
WT
ΔccmA
ΔNT
ΔMM
Δ13-17
ΔCT
BD
D
WT CcmA
ΔccmA
ΔNT
ΔMM
Δ13-17
ΔCT
BD
Frequency
Side Curvature

Figure 3

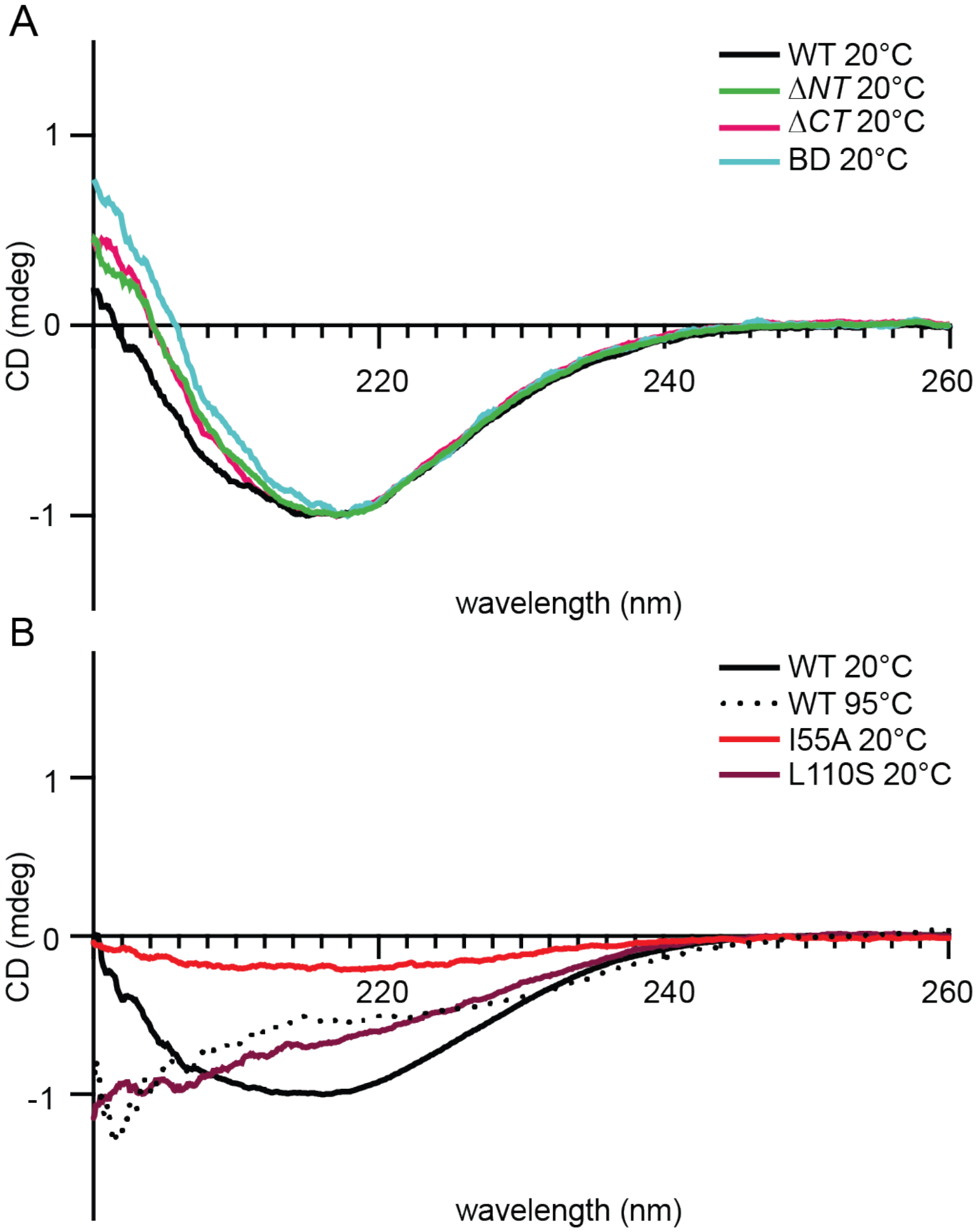
A
WT 20°C
ΔNT 20°C
ΔCT 20°C
BD 20°C
1
0
-1
CD (mdeg)
220
240
260
wavelength (nm)
B
WT 20°C
WT 95°C
I55A 20°C
L110S 20°C
1
0
-1
CD (mdeg)
220
240
260
wavelength (nm)

Figure 4

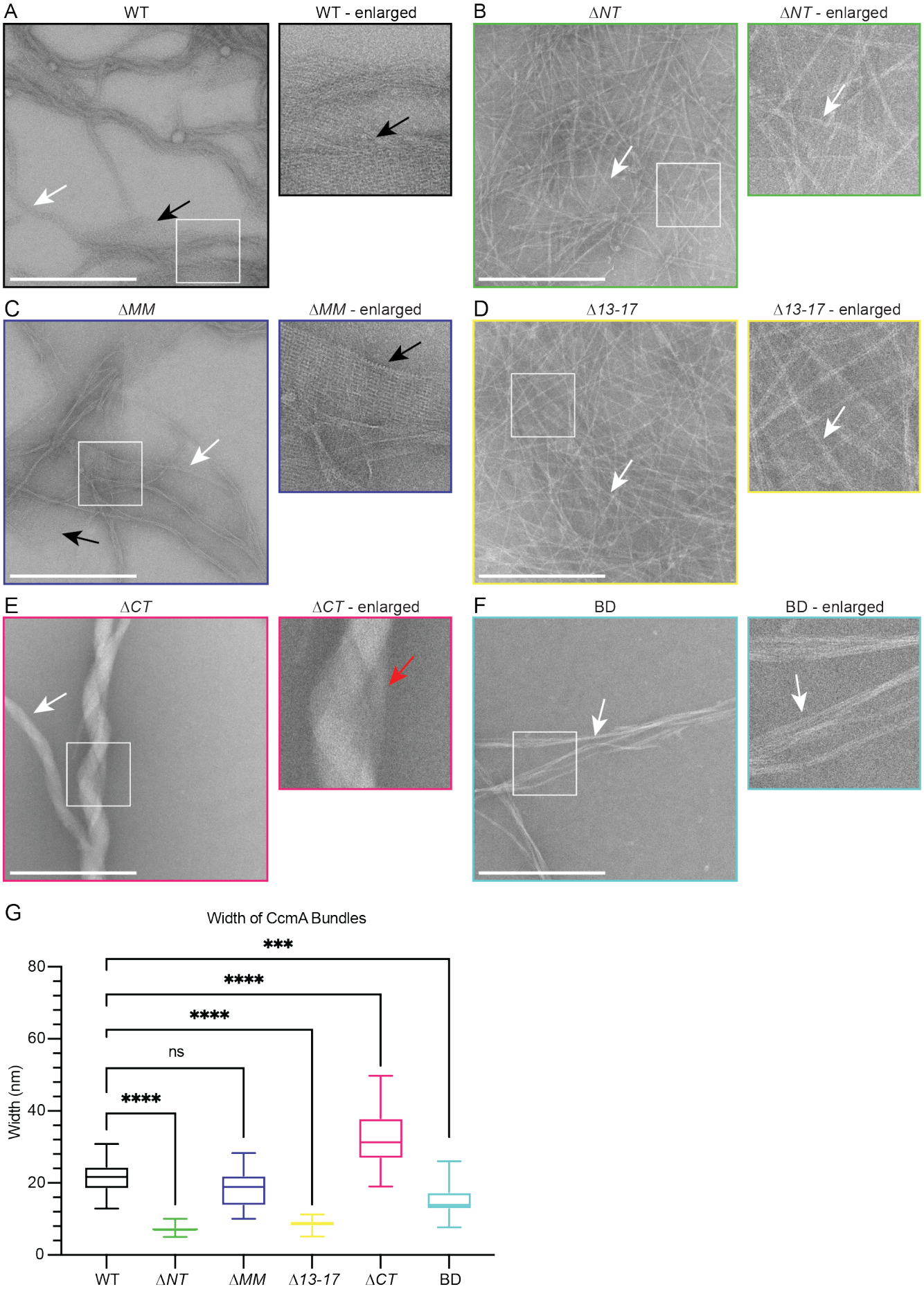
A
WT
WT - enlarged
B
ΔNT
ΔNT - enlarged
C
ΔMM
ΔMM - enlarged
D
Δ13-17
Δ13-17 - enlarged
E
ΔCT
ΔCT - enlarged
F
BD
BD - enlarged
G
Width of CcmA Bundles
Width (nm)
0
20
40
60
80
***
****
****
ns
****
WT
ΔNT
ΔMM
Δ13-17
ΔCT
BD

Figure 5

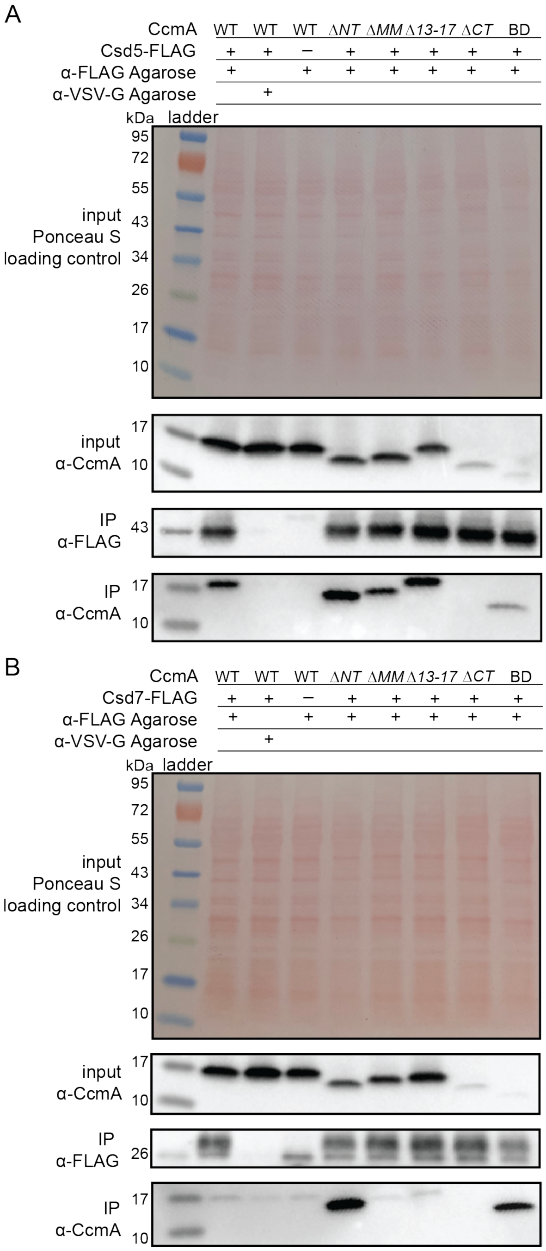
A
CcmA WT WT WT ΔNT ΔMM Δ13-17 ΔCT BD
Csd5-FLAG + + − + + + + +
α-FLAG Agarose + + + + + + +
α-VSV-G Agarose +
kDa ladder
95
72
55
43
34
26
17
10
input
Ponceau S
loading control
input
α-CcmA
17
10
IP
α-FLAG
43
IP
α-CcmA
17
10
B
CcmA WT WT WT ΔNT ΔMM Δ13-17 ΔCT BD
Csd7-FLAG + + − + + + + +
α-FLAG Agarose + + + + + + +
α-VSV-G Agarose +
kDa ladder
95
72
55
43
34
26
17
10
input
Ponceau S
loading control
input
α-CcmA
17
10
IP
α-FLAG
26
IP
α-CcmA
17
10

Figure 6

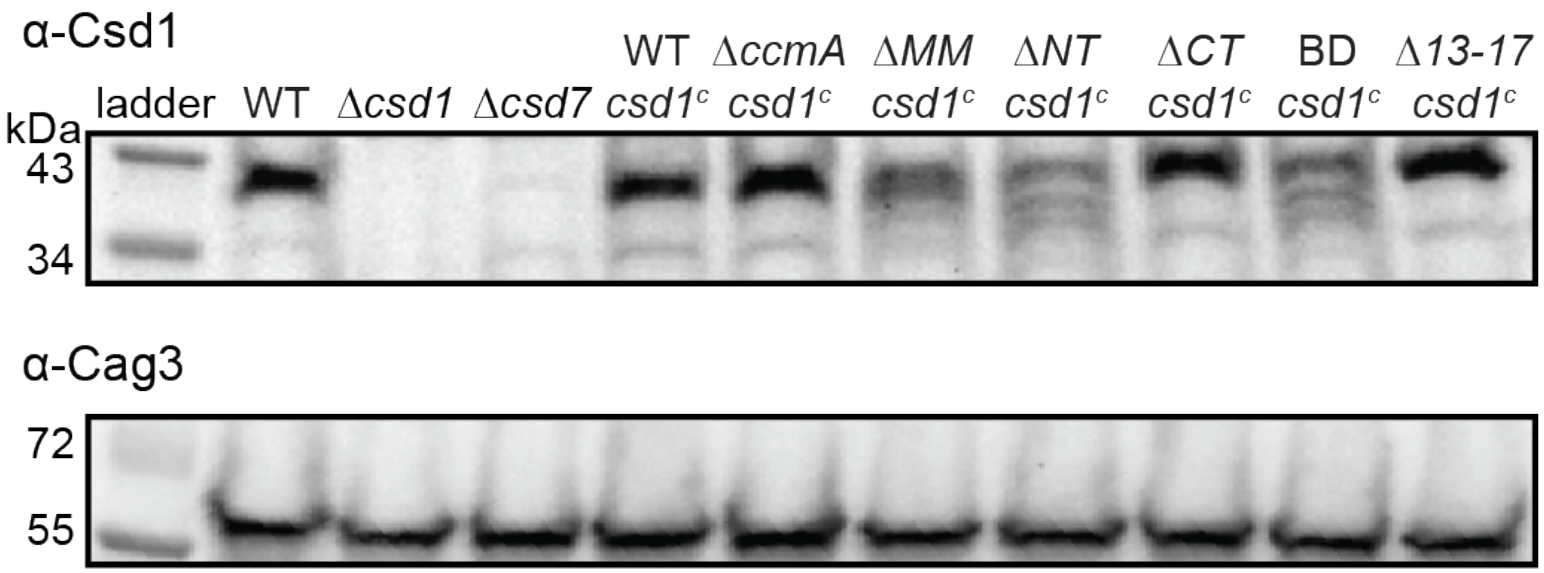
α-Csd1
ladder
WT
Δcsd1
Δcsd7
WT csd1c
ΔccmA csd1c
ΔMM csd1c
ΔNT csd1c
ΔCT csd1c
BD csd1c
Δ13-17 csd1c
kDa
43
34
α-Cag3
72
55

Figure 7

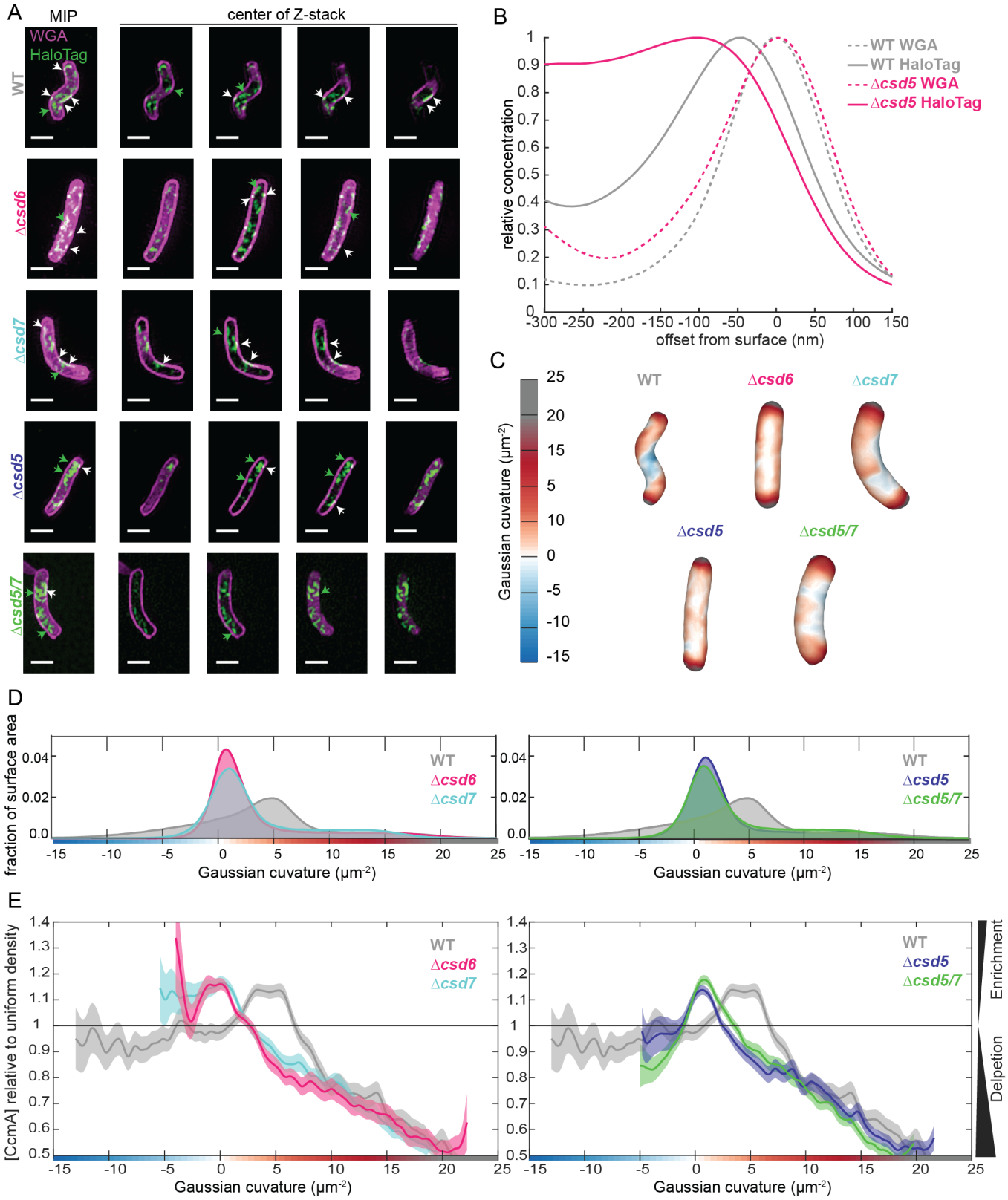
A
MIP
center of Z-stack
WGA
HaloTag
WT
Δcsd6
Δcsd7
Δcsd5
Δcsd5/7
B
relative concentration
offset from surface (nm)
WT WGA
WT HaloTag
Δcsd5 WGA
Δcsd5 HaloTag
C
Gaussian cuvature (μm-2)
WT
Δcsd6
Δcsd7
Δcsd5
Δcsd5/7
D
fraction of surface area
Gaussian cuvature (μm-2)
WT
Δcsd6
Δcsd7
Δcsd5
Δcsd5/7
E
[CcmA] relative to uniform density
Gaussian cuvature (μm-2)
Enrichment
Delpetion

Figure 8

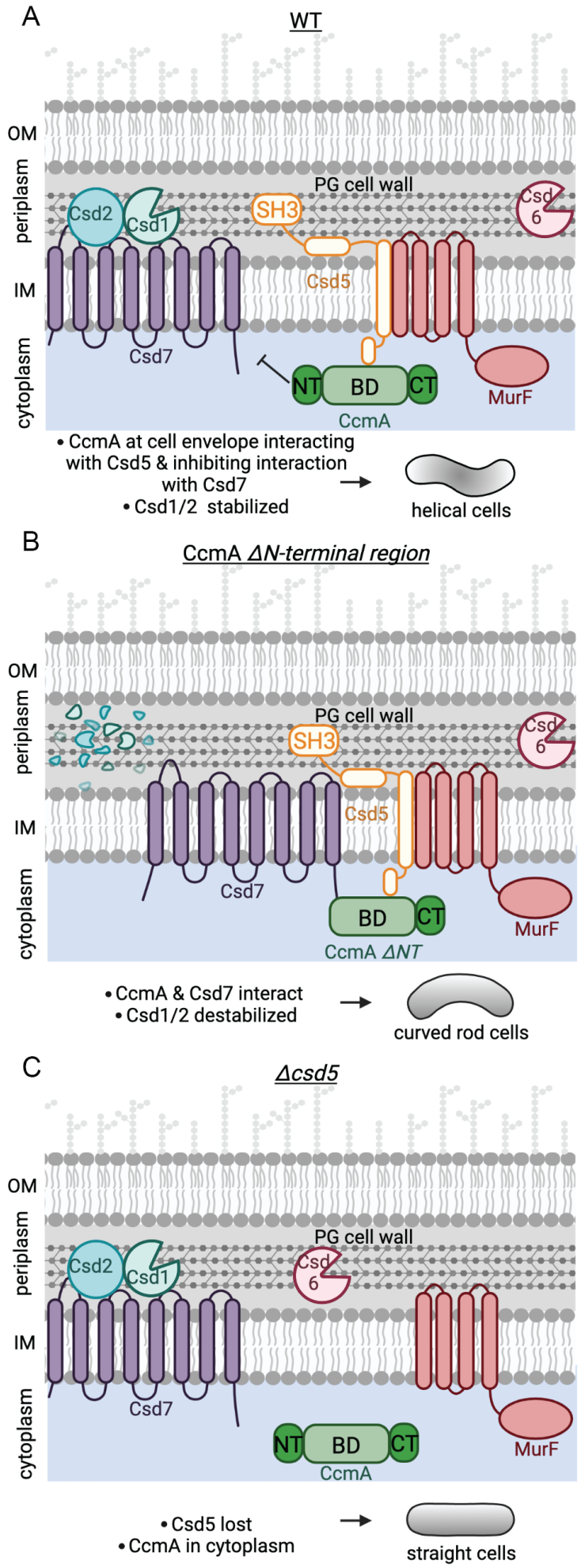
A
WT
OM
periplasm
IM
cytoplasm
PG cell wall
Csd2
Csd1
SH3
Csd 6
Csd5
Csd7
NT
BD
CT
CcmA
MurF
• CcmA at cell envelope interacting with Csd5 & inhibiting interaction with Csd7
• Csd1/2 stabilized
helical cells
B
CcmA ΔN-terminal region
OM
periplasm
IM
cytoplasm
PG cell wall
SH3
Csd 6
Csd5
Csd7
BD
CT
CcmA ΔNT
MurF
• CcmA & Csd7 interact
• Csd1/2 destabilized
curved rod cells
C
Δcsd5
OM
periplasm
IM
cytoplasm
PG cell wall
Csd2
Csd1
Csd 6
Csd7
NT
BD
CT
CcmA
MurF
• Csd5 lost
• CcmA in cytoplasm
straight cells